

EVIDENCE FOR MERGER-DRIVEN GROWTH IN LUMINOUS, HIGH-Z, OBSCURED AGN IN THE CANDELS/COSMOS FIELD

J. L. DONLEY¹, J. KARTALTEPE², D. KOCEVSKI³, M. SALVATO⁴, P. SANTINI⁵, H. SUH⁶, F. CIVANO⁷, A. M. KOEKEMOER⁸, J. TRUMP⁹, M. BRUSA¹⁰, C. CARDAMONE¹¹, A. CASTRO^{12,13}, M. CISTERNAS¹⁴, C. CONSELICE¹⁵, D. CROTON¹⁶, N. HATHI^{17,8}, C. LIU^{18,19,20}, R. A. LUCAS⁸, P. NAIR²¹, D. ROSARIO⁴, D. SANDERS²², B. SIMMONS^{23,24}, C. VILLFORTH^{25,26}, D. M. ALEXANDER²⁷, E. F. BELL²⁸, S. M. FABER²⁹, N. A. GROGIN⁸, J. LOTZ⁸, D. H. MCINTOSH³⁰, T. NAGAO³¹

¹Los Alamos National Laboratory, P.O. Box 1663, Los Alamos, NM 87545 jdonley@lanl.gov

²Rochester Institute of Technology, Rochester, NY, USA

³Colby College, Waterville, Maine 04901

⁴Max Planck Institut für extraterrestrische Physik, Giessenbachstrasse 1, D-85748 Garching bei München, Germany

⁵INAF-Osservatorio Astronomico di Roma, via di Frascati 33, I-00040, Monte Porzio Catone, Roma, Italy

⁶Subaru Telescope, National Astronomical Observatory of Japan, 650 A'ohoku place, Hilo, HI, 96720, USA

⁷Harvard-Smithsonian Center for Astrophysics, 60 Garden Street, Cambridge, MA 02138, USA

⁸Space Telescope Science Institute, 3700 San Martin Drive, Baltimore, MD 21218

⁹University of Connecticut, 2152 Hillside Road, U-3046, Storrs, CT 06269

¹⁰INAF-Osservatorio Astronomico di Bologna, via Ranzani 1, I-40127, Bologna, Italy

¹¹Department of Math & Science, Wheelock College, 200 Riverway, Boston, MA 02215, USA

¹²Universidad Nacional Autónoma de México (UNAM), Instituto de Astronomía, Observatorio Astronómico Nacional. A.P. 877, 22800 Ensenada, BC, México

¹³Universidad Autónoma de Ciudad Juárez, Instituto de Ingeniería y Tecnología. 1210 Plutarco Elias Calles, 32310 Cd. Juárez, CH, México

¹⁴Instituto de Astrofísica de Canarias, E-38205 La Laguna, Tenerife, Spain

¹⁵School of Physics & Astronomy, University of Nottingham, Nottingham, NG7 2RD, UK

¹⁶Centre for Astrophysics & Supercomputing, Swinburne University of Technology, P.O. Box 218, Hawthorn, Victoria 3122, Australia

¹⁷Aix Marseille Université, CNRS, LAM (Laboratoire d'Astrophysique de Marseille) UMR 7326, 13388, Marseille, France

¹⁸Astrophysical Observatory, Department of Engineering Science and Physics, City University of New York, College of Staten Island, 2800 Victory Boulevard, Staten Island, NY 10314

¹⁹Department of Astrophysics and Hayden Planetarium, American Museum of Natural History, New York, NY 10024

²⁰Physics Program, The Graduate Center, CUNY, New York, NY 10016

²¹Department of Physics and Astronomy, University of Alabama, Box 870324, Tuscaloosa, AL 35487-0324, USA

²²Institute for Astronomy, University of Hawaii, 2680 Woodlawn Drive, Honolulu, HI 96822, USA

²³Center for Astrophysics and Space Sciences, University of California, San Diego, La Jolla, CA 92093, USA

²⁴Einstein Fellow

²⁵University of Bath, Department of Physics, Claverton Down, Bath, BA2 7AY, UK

²⁶Scottish University Physics Alliance (SUPA), University of St Andrews, North Haugh, KY16 9SS, St Andrews, UK

²⁷Centre for Extragalactic Astronomy, Department of Physics, Durham University, South Road, Durham DH1 3LE, UK

²⁸Department of Astronomy, University of Michigan, Ann Arbor, MI 48109, USA

²⁹Department of Astronomy and Astrophysics, University of California Observatories/Lick Observatory, University of California, Santa Cruz, CA 95064, USA

³⁰Department of Physics and Astronomy, University of Missouri-Kansas City, Kansas City, MO 64110, USA

³¹Research Center for Space and Cosmic Evolution, Ehime University, Bunkyo-cho 2-5, Matsuyama, Ehime 790-8577, Japan

ABSTRACT

While major mergers have long been proposed as a driver of both AGN activity and the $M_{\text{BH}} - \sigma_{\text{bulge}}$ relation, studies of moderate to high redshift Seyfert-luminosity AGN hosts have found little evidence for enhanced rates of interactions. However, both theory and observation suggest that while these AGN may be fueled by stochastic accretion and secular processes, high-luminosity, high-redshift, and heavily obscured AGN are the AGN most likely to be merger-driven. To better sample this population of AGN, we turn to infrared selection in the CANDELS/COSMOS field. Compared to their lower-luminosity and less obscured X-ray-only counterparts, IR-only AGN (luminous, heavily obscured AGN) are more likely to be classified as either irregular ($50^{+12}_{-12}\%$ vs. $9^{+5}_{-2}\%$) or asymmetric ($69^{+9}_{-13}\%$ vs. $17^{+6}_{-4}\%$) and are less likely to have a spheroidal component ($31^{+13}_{-9}\%$

vs. $77^{+4}_{-6}\%$). Furthermore, IR-only AGN are also significantly more likely than X-ray-only AGN ($75^{+8}_{-13}\%$ vs. $31^{+6}_{-6}\%$) to be classified either as interacting or merging in a way that significantly disturbs the host galaxy or disturbed though not clearly interacting or merging, which potentially represents the late stages of a major merger. This suggests that while major mergers may not contribute significantly to the fueling of Seyfert luminosity AGN, interactions appear to play a more dominant role in the triggering and fueling of high-luminosity heavily obscured AGN.

Keywords: galaxies: active — infrared: galaxies — X-rays: galaxies

1. INTRODUCTION

The origin of the evolutionary connection between supermassive black holes (SMBHs) and their host galaxies, as evidenced by the $M_{\text{BH}} - \sigma_{\text{bulge}}$ relation (Magorrian et al. 1998; Gebhardt et al. 2000), remains one of the major open questions in extragalactic astronomy. For the past decade, theorists have invoked major mergers between gas-rich galaxies to explain not only this correlation, but also the strikingly similar cosmic evolution of AGN and star-formation activity (e.g., Hopkins et al. 2008).

Not only are major mergers required to reproduce the properties of classical bulges in simulations of galaxy formation, but when coupled with feedback, mergers can reproduce many of the global properties of both the AGN and galaxy populations, including the $M_{\text{BH}} - \sigma_{\text{bulge}}$ relation (Di Matteo et al. 2005; Robertson et al. 2006; Hopkins et al. 2006, 2008). Furthermore, the best examples of ongoing mergers in the local Universe, ultraluminous infrared galaxies (ULIRGS), have long been known to be active sites of both intense star-formation and AGN activity. This observation led to a proposed co-evolutionary scenario in which major mergers drive the growth of bulges via nuclear star-formation and violent relaxation, and provide fuel to a rapidly accreting AGN via merger-induced gravitational torques (Sanders et al. 1988; Hopkins et al. 2008).

At first glance, studies of local ($z < 0.45$) QSOs appear to support this scenario, with 25-100% showing evidence for ongoing mergers or tidal debris (Bahcall et al. 1997; Canalizo & Stockton 2001; Zakamska et al. 2006; Bennert et al. 2008; Greene et al. 2009; Veilleux et al. 2009a). While these small targeted studies indicate that local QSOs are commonly associated with mergers, the few studies that compare their morphologies to inactive control samples fail to find evidence for enhanced morphological disturbances (Dunlop et al. 2003; Reichard et al. 2009). QSOs, however, are rare in the local Universe, and may not be triggered by the same mechanisms responsible for driving their high-redshift counterparts onto the $M_{\text{BH}} - \sigma_{\text{bulge}}$ relation, which was largely in place by $z \sim 1$ (e.g., Cisternas et al. 2011a). To determine the prevalence of mergers among high-redshift AGN, we have therefore turned to the cosmological deep fields.

Studies of AGN hosts in the GEMS, GOODS, AEGIS, and COSMOS fields have predominantly targeted X-ray selected AGN at $0.2 < z < 1.3$ (Sánchez et al. 2004; Grogin et al. 2005; Pierce et al. 2007; Gabor et al. 2009; Cisternas et al.

2011b; Simmons et al. 2012; Villforth et al. 2014; Rosario et al. 2015; Bruce et al. 2016). While a small fraction of these AGN hosts show strong distortions, the rate of morphological disturbances is similar to that of inactive galaxy control samples, suggesting that mergers do not play a dominant role in AGN fueling, at least out to $z \sim 1$. That said, there is evidence for a factor of ~ 2.5 enhancement of Seyfert-level AGN activity in close pairs (Silverman et al. 2011; Ellison et al. 2011) and evidence that minor mergers may play a role in the fueling of moderate-luminosity AGN (Altamirano-Dévora et al. 2016). Furthermore, Koss et al. (2010) find both an increased pair and merger fraction in local hard X-ray AGN samples.

To extend this analysis to the peak of AGN activity at $z \sim 2$, we turn to the near-IR HST/WFC3 CANDELS survey, which probes light redward of the 4000 Å break and thus traces emission from the stars responsible for the bulk of the stellar mass. Initial studies of the hosts of $z \sim 2$ X-ray AGN in the GOODS-S region of CANDELS, however, likewise find morphologies that are indistinguishable from those of normal star-forming galaxies (Schawinski et al. 2011; Kocevski et al. 2012; Simmons et al. 2012). Furthermore, the high incidence of disk galaxies, which should be destroyed by major mergers, suggests that a time delay between merger activity and the AGN phase cannot account for the lack of merger signatures.

While these observations appear to call into question the role of major mergers in AGN/galaxy co-evolution, most X-ray AGN populations studied thus far are dominated by low-luminosity Seyfert galaxies ($\log L_{0.5-10\text{keV}}$ (ergs s⁻¹) < 44), which may be experiencing a different mode of SMBH and galaxy growth than their high-luminosity counterparts. For instance, while cosmological simulations require mergers to reproduce the properties of luminous QSOs, stochastic accretion and secular processes can account for the lower levels of nuclear activity in Seyfert galaxies (Hopkins & Hernquist 2006; Hopkins et al. 2008; Hasinger 2008; Hopkins & Hernquist 2009; Hopkins et al. 2014). This hypothesis appears to be backed by a growing number of studies that find a larger merger-driven and disturbed fraction among high luminosity AGN across a range of redshifts (Guyon et al. 2006; Urrutia et al. 2008; Kartaltepe et al. 2010; Koss et al. 2012; Treister et al. 2012; Glikman et al. 2015; Ellison et al. 2016; Fan et al. 2016), though there are exceptions (Villforth et al. 2014; Mechtley et al. 2016; Villforth et al. 2017). A similar trend has been observed in both the local and high- z infrared and

SMG galaxy populations, where late-stage major mergers are responsible for fueling nearly all of the most luminous galaxies (Larson et al. 2016; Engel et al. 2010; Ivison et al. 2012).

If the merger-driven evolutionary scenarios summarized in Hopkins et al. (2008) and Alexander & Hickox (2012) are correct, the early phases of a major merger should be dominated by luminous, yet heavily obscured, AGN activity. As the SMBH grows, AGN feedback then serves to remove the dust and gas and the AGN becomes dust reddened and eventually unobscured, but only after the fading merger features become difficult to identify, particularly in the distant universe. To test the major merger scenario for the co-evolution of SMBHs and their hosts, studies should therefore target not only luminous AGN, but heavily obscured luminous AGN. While doing so can be difficult using soft X-ray and optical emission alone, the same dust and gas that serves to obscure the AGN’s signatures also acts like a natural coronagraph, blocking the intense UV-optical radiation from the AGN itself and permitting a study of the underlying host galaxy emission.

A number of studies have begun to target obscured AGN at both low and high luminosity, and most (Schawinski et al. 2012 is an exception) have indeed found a higher rate of disturbances among more heavily obscured samples (Koss et al. 2010; Urrutia et al. 2012; Satyapal et al. 2014; Kocevski et al. 2015; Ellison et al. 2016; Shangguan et al. 2016; Fan et al. 2016; Weston et al. 2017) or evidence that extinction peaks during the intermediates stages of merger evolution (Veilleux et al. 2009b), albeit with a strong chaotic component. This suggests that AGN unification is not due solely to orientation (Cattaneo et al. 2005; Kocevski et al. 2015).

High luminosity, high redshift, and heavily obscured AGN therefore comprise the population of AGN most likely to experience merger-driven SMBH and galaxy co-evolution. Fortunately, these AGN can effectively be targeted using their mid-IR colors. For an AGN to be identified via its MIR colors, its hot dust emission must overpower the underlying stellar emission from the host galaxy (e.g., Donley et al. 2008, 2012). MIR selection therefore identifies the most luminous, and thus the highest-redshift ($z \sim 2$) AGN in the limited volumes probed by deep survey fields, recovering few Seyfert galaxies but $> 75\%$ of X-ray AGN with QSO luminosities (Donley et al. 2012). Furthermore, because NIR-MIR emission is largely insensitive to intervening obscuration, the unique MIR power-law signature of luminous AGN is observable in both unobscured and heavily obscured AGN. MIR selection therefore provides a way to recover highly complete samples of luminous, high- z , and heavily obscured AGN, exactly those AGN whose evolution is expected to be dominated by major mergers (Alonso-Herrero et al. 2006; Donley et al. 2007, 2010, 2012).

In the work that follows, we directly compare for the first time the morphologies of X-ray and infrared selected AGN. If mergers do indeed play a dominant role in the triggering

of luminous, high- z , obscured AGN, we should see an excess of merger signatures in our sample of high-luminosity, heavily obscured IR-only AGN when compared to the lower-luminosity, less heavily-obscured X-ray-only population.

This paper is organized as follows. In §2 we discuss the relevant data in the CANDELS/COSMOS field and describe our selection of the infrared and X-ray AGN samples. The sample properties (reliability, redshifts, luminosities, and stellar masses) are given in §3. In §4 we present the visual classification scheme as well as the resulting morphologies for the infrared and X-ray AGN samples. The conclusions are given in §5. Throughout the paper, we assume the following cosmology: $(\Omega_m, \Omega_\Lambda, H_0) = (0.27, 0.73, 70.5 \text{ km s}^{-1} \text{ Mpc}^{-1})$.

2. DATA AND SAMPLE SELECTION

We selected the AGN for this study from the ~ 200 sq. arcmin CANDELS/COSMOS field. The CANDELS survey imaged the central region of the COSMOS field in both the WFC3 F125W (J-band) and F160W (H-band) filters to 5σ limiting AB magnitudes of 27.72 and 27.56, respectively (see Koekemoer et al. 2011 and Nayyeri et al. 2017 for details on the CANDELS HST data products). This high resolution NIR imaging data provides a crucial look at the rest-frame optical emission from moderate to high redshift galaxies and AGN.

The COSMOS survey provides ample multiwavelength data over the field, including the X-ray (*XMM* and *Chandra*) and MIR (*Spitzer* IRAC) coverage most relevant to this work. Shallow (~ 40 ks) *XMM* data extends over the full COSMOS field (Hasinger et al. 2007; Cappelluti et al. 2009; Brusa et al. 2010), whereas the deeper *Chandra* coverage used here is limited to the central 0.9 deg^2 , but fully covers the CANDELS/COSMOS field with an average exposure time of ~ 170 ks. (Deeper *Chandra* data now exist in the outer regions of the COSMOS field (Civano et al. 2016), but do not overlap the CANDELS field.)

The primary *Spitzer* IRAC data used for this study (Sanders et al. 2007) cover the full COSMOS field to 1200s depth, or 5σ sensitivities of 0.9, 1.7, 11.3, and $14.6 \mu\text{Jy}$ in the 3.6, 4.5, 5.8, and $8.0 \mu\text{m}$ bands, respectively. We exclude from our study all IRAC sources that lie within the masked regions of bright ($K < 14$) 2MASS sources, but include sources with flags indicating nearby neighbors or deblending. Of the ~ 1000 IRAC sources that fall within the CANDELS/COSMOS field and that are brighter than the 5σ sensitivities in each of the IRAC bands, 9% have either bad pixels or neighbors bright and close enough to significantly bias the photometry and 11% were originally blended with another object (note: these are not mutually exclusive). Of the 43 infrared-selected AGN (IRAGN) we will select using this data, 5 (12%) are flagged as having nearby neighbors or were blended with another object, but a careful inspection of each source indicates that the IRAGN selection is robust to

these issues. Furthermore, our comparison below with the COSMOS15 IRAC photometry (see §3.1) provides an additional check on the IRAGN selection reliability.

2.1. IRAGN

IRAGN were selected directly from the Sanders et al. (2007) IRAC catalog using the criteria outlined in Donley et al. (2012):

$$x = \log_{10} \left(\frac{f_{5.8\mu\text{m}}}{f_{3.6\mu\text{m}}} \right), \quad y = \log_{10} \left(\frac{f_{8.0\mu\text{m}}}{f_{4.5\mu\text{m}}} \right) \quad (1)$$

$$x \geq 0.08 \quad \wedge \quad y \geq 0.15 \quad (2)$$

$$\wedge \quad y \geq (1.21 \times x) - 0.27 \quad \wedge \quad y \leq (1.21 \times x) + 0.27$$

$$\wedge \quad f_{4.5\mu\text{m}} > f_{3.6\mu\text{m}} \quad \wedge \quad f_{5.8\mu\text{m}} > f_{4.5\mu\text{m}} \quad \wedge \quad f_{8.0\mu\text{m}} > f_{5.8\mu\text{m}}$$

As in Donley et al. (2012), we require that IRAGN have fluxes that exceed the 5σ sensitivities in each of the IRAC bands (see above). We experimented with loosening this criterion, but the vast majority of additional sources we select were not clearly visible in one of either the $5.8\mu\text{m}$ or $8.0\mu\text{m}$ bands. In total, we identify 43 IRAGN across the CANDELS/COSMOS field. We cross-check the IRAGN selected using the Sanders et al. (2007) catalog against those selected using the Laigle et al. (2016) COSMOS15 catalog in §3.1 below.

After selecting the IRAGN, we located the nearest CANDELS H-band source using a search radius of $2''$. By directly matching the IRAC and H-band catalogs, we avoided imposing a criterion that there be a visible (I-band) counterpart. In most cases, this made no practical difference, but for 3 IRAGN, the nearest H-band source has no corresponding optical counterpart in the Subaru I-band catalog of Ilbert et al. (2009). In contrast, all IRAGN had an H-band counterpart, with median and maximum offsets of $0.12''$ and $0.56''$, respectively.

2.2. X-ray AGN

X-ray AGN were selected from the *Chandra* catalog of Civano et al. (2012).¹ We match the H-band catalog directly to the X-ray positions. Of the 99 *Chandra* sources, all but 3 have a clear H-band counterpart within the $2''$ radius. One of these sources is later removed from our sample because it falls below our X-ray luminosity cut. For the remaining two sources, we searched for an H-band counterpart using the optical counterpart position given in Civano et al. (2012). One

has an H-band counterpart only $0.11''$ from the optical position, the other has no H-band counterpart, and is therefore excluded from our study.

Starting from the H-band, as opposed to the optical I-band, allowed us to identify clear counterparts for 4 *Chandra* sources that have no Subaru optical counterpart (Ilbert et al. 2009) in Civano et al. (2012). For the remaining sources, the optical counterpart nearest our H-band counterpart matches the optical counterpart identified by Civano et al. (2012).

3. SAMPLE PROPERTIES

Our full sample of X-ray and infrared-selected AGN consists of 43 IRAGN, 16 of which have no X-ray counterpart, and 72 *Chandra* or XMM-selected AGN that are *not* IRAGN (or that fall below the IRAC flux cuts in one or more of the IRAC bands). IRAGN selection predominantly identifies the most intrinsically luminous AGN (see §3.4), and the IRAGN lacking X-ray counterparts are likely to be luminous but heavily obscured (Donley et al. 2012). In contrast, the X-ray-only sample should predominantly lie at lower luminosities and/or redshifts and be dominated by sources with low to moderate obscurations. As such, it will serve as our control sample for comparison to the higher luminosity and higher-redshift IRAGN.

3.1. IRAGN Selection Reliability

To check the reliability of the IRAGN selected using the Sanders et al. (2007) catalog, we turn to the COSMOS15 catalog (Laigle et al. 2016), a NIR-based catalog with PSF-matched photometry from the UV to the MIR. COSMOS15 takes advantage of the deeper data in IRAC channels 1 and 2 provided by the SEDS and SPLASH COSMOS surveys (see Capak et al. 2017, in prep), but uses the same data presented in Sanders et al. (2007) for IRAC channels 3 and 4. However, for these two longer-wavelength channels, the error estimates from COSMOS15 are far more conservative than those given by Sanders et al. (2007), and the agreement between the catalogs begins to break down for sources with moderate Sanders et al. (2007) S/N but COSMOS15 $S/N < 3$ in one or more of the IRAC bands.

If we require that our IRAGN be selected as such based on both the Sanders et al. (2007) and COSMOS15 catalogs, our sample of X-ray-detected IRAGN drops by four from 27 to 23. The four sources that are lost all have COSMOS15 $S/N > 3$ in each of the IRAC bands, but the modest differences in photometry tend to place the Sanders et al. (2007)-selected IRAGN just outside of the selection box.

Because X-ray undetected IRAGN tend to be fainter than their X-ray-detected counterparts, the discrepancy between the catalogs at low COSMOS15 S/N has a far larger effect on our sample of X-ray undetected IRAGN. Of the 16 Sanders et al. (2007)-selected IRAGN without X-ray counterparts, only 7 would also be selected as IRAGN using the COSMOS15 photometry (all 7 have COSMOS15 $S/N > 3$

¹ 60 sources in our sample have XMM counterparts from Brusa et al. (2010). Of these, all but 6 have *Chandra* counterparts. We carefully examined these six sources, and found that only one, also an IRAGN, had a visible excess of *Chandra* counts near the XMM source position. While we therefore consider this source to be X-ray detected, we exclude the remaining XMM-only sources from our sample as all are detected in only one of the XMM bands (full/hard/soft) to $\leq 6\sigma$. This choice has no effect on the final conclusions of this work.

in each IRAC band). We make the case below for keeping an additional 2 sources, bringing the number of X-ray undetected AGN to 9, but the cross-check with COSMOS15 may remove as many as 7 of the 16 IRAGN identified by [Sanders et al. \(2007\)](#).

Of these 7 IRAGN not selected using COSMOS15, 5 have a COSMOS15 $S/N \lesssim 3$ in IRAC channel 4 and largely discrepant channel 4 fluxes between the two catalogs, and 2 have $S/N > 3$ but were already marginal IRAGN. Whether these sources are indeed IRAGN or not therefore appears to be catalog-dependent, and we will consider both cases in the analysis below. As for the remaining two X-ray-undetected IRAGN not identified by COSMOS15, one lacks a COSMOS15 counterpart altogether but has a high [Sanders et al. \(2007\)](#) S/N in all IRAC bands and the other is a single IRAC source whose flux appears to have been split between two optical/NIR counterparts in COSMOS15. Furthermore, for the latter, only its slightly non-monotonic COSMOS15 IRAC fluxes cause it to not meet our strict IRAGN criteria: its COSMOS15 photometry places it inside the IRAGN selection box. We therefore keep both IRAGN in our COSMOS15 sample, which can generally be viewed as a higher S/N sub-sample of the full [Sanders et al. \(2007\)](#)-selected IRAGN sample. The impact of this IRAC S/N cut on our results will be discussed below in §4.1.

3.2. Redshifts

Of the 115 AGN in our full sample, 69 have spectroscopic redshifts from either public or internal COSMOS team datasets obtained using the following instruments or surveys: DEIMOS (Keck), FMOS (Subaru), FORS1 (VLT), FORS2 (VLT), FOCAS, HST Grism, IMACS (Magellan), LRIS (Keck), MOSFIRE (Keck), PRIMUS (Magellan/IMACS), SDSS, VIMOS (zCOSMOS), XSHOOTER (VLT), and 3DHST. The spectroscopic redshift fraction is $\sim 60\%$ for both the IRAGN and X-ray-only samples. For the remaining X-ray detected AGN with optical counterparts, we adopt the AGN-specific photometric redshifts calculated by [Salvato et al. \(2011\)](#), and for the IRAGN lacking X-ray counterparts, we calculate photometric redshifts using the methods outlined in [Salvato et al. \(2011\)](#) for consistency. Doing so gives redshift measurements or estimates for all but the 3 IRAGN and 4 X-ray-only AGN that lack clear optical counterparts. The median redshifts for the [Sanders et al. \(2007\)](#) and COSMOS15 IRAGN samples are $z = 1.93$ and $z = 1.87$, respectively, and that of the X-ray-only sample is $z = 1.22$.

3.3. Observed X-ray Luminosities

We plot in Figure 1 the redshifts and observed 0.5-10 keV X-ray luminosities for our AGN samples. We have excluded from the X-ray-only sample 4 X-ray sources with luminosities lower than 10^{42} erg s $^{-1}$. We also identify in Figure 1 those AGN that meet the IRAGN criteria.

As can be seen in Figure 1, 80% of the high luminosity

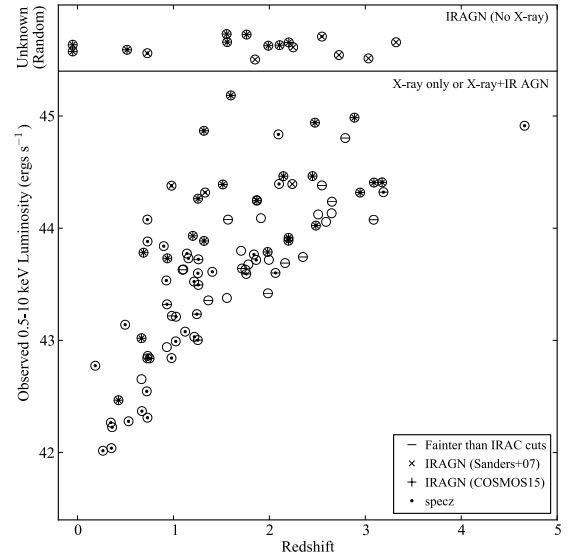


Figure 1. Observed 0.5-10 keV X-ray luminosity vs. redshift for the IR and X-ray selected AGN. IR-only AGN are shown on the top, where their unknown “X-ray luminosity” has been randomized for plotting purposes and sources with unknown redshifts are assigned a value of -0.1. The vast majority of high-luminosity X-ray AGN are also selected as IRAGN, whereas most X-ray-only AGN are Seyfert galaxies.

($L_x > 10^{44}$ erg s $^{-1}$) X-ray AGN with good IRAC fluxes are also IRAGN. In contrast, only 25% of the lower-luminosity ($L_x < 10^{44}$ erg s $^{-1}$) X-ray AGN with good IRAC fluxes are IRAGN, and 80% of these have X-ray luminosities greater than 5×10^{43} erg s $^{-1}$. As expected, the IRAGN selection effectively identifies the highest luminosity AGN, whereas the X-ray selection is sensitive to lower-luminosity Seyfert galaxies.

3.4. Bolometric Luminosities

Using the COSMOS15 catalog and the SED-fitting approach of [Suh et al. \(2017\)](#), which requires both a redshift and a $24\mu\text{m}$ detection, we calculate the AGN bolometric luminosity for 76 of the 111 AGN in our sample. The requirements listed above exclude 4 IR-only AGN (one with no COSMOS15 counterpart, one with no redshift, and two that are blended with brighter nearby sources and so have no reported $24\mu\text{m}$ fluxes), as well as 31 X-ray sources (2 with no COSMOS15 counterpart, 4 with no redshift, and 25 with no $24\mu\text{m}$ counterpart).

For X-ray AGN with redshifts, we can also estimate the AGN bolometric luminosity using the absorption-corrected rest-frame 0.5-10 keV X-ray luminosities from [Marchesi et al. \(2016a\)](#) and [Marchesi et al. \(2016b\)](#), where we give preference to the results from X-ray spectral fitting ([March-](#)

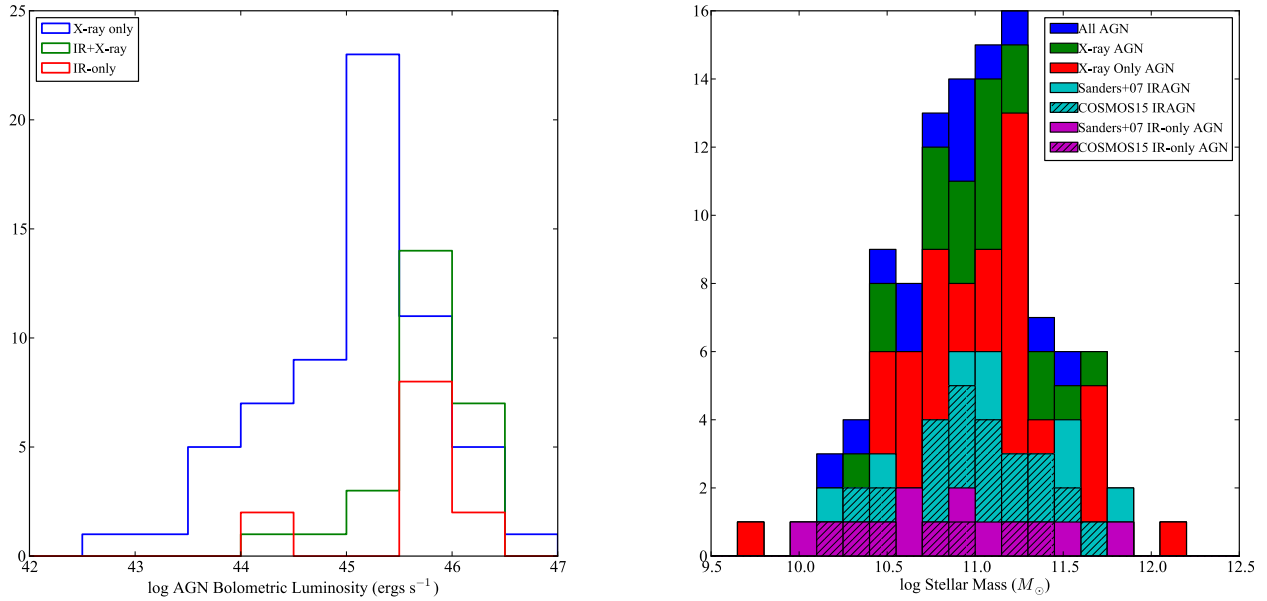


Figure 2. Left: AGN bolometric luminosity for the IR-only, IR+X-ray, and X-ray-only AGN populations. Bolometric luminosities were derived from SED fitting for sources with $24\mu\text{m}$ counterparts, and from the X-ray luminosity for sources without $24\mu\text{m}$ counterparts. IRAGN selection preferentially identifies the most intrinsically luminous AGN. Right: stellar mass distribution for the various AGN subsamples, which are consistent with having been drawn from the same population.

esi et al. 2016b) when they are available² (Note: for sources with only an upper limit on N_{H} , we apply no absorption correction, and for sources with only a lower limit on N_{H} , we apply the correction associated with this lower limit.) Of the 94 *Chandra* sources in our sample, 62 have both an SED-derived bolometric luminosity as well as an X-ray luminosity. Comparing the AGN luminosities for this subsample gives an X-ray bolometric correction of $k_{\text{bol}} = 44$, in agreement with Hopkins et al. (2007) for an AGN sample with the median bolometric luminosity of our sample: $11.9 L_{\odot}$. The scatter about the resulting $L_{\text{bol}}(\text{SED})$ vs. $L_{\text{bol}}(\text{X-ray})$ relation has a standard deviation of $\sigma(\log L_{\text{bol}}) = 0.45$. Using this bolometric correction, we estimate the AGN bolometric luminosity for the remaining 26 X-ray sources in our sample with a redshift but no $24\mu\text{m}$ counterpart. Combining these X-ray-derived AGN bolometric luminosities with the SED-derived AGN bolometric luminosities gives the distributions shown in Figure 2, where we give preference to the SED-derived L_{bol} when it is available.

As expected, and as was demonstrated using the X-ray luminosities in Figure 1 for AGN with X-ray counterparts, IRAGN selection preferentially identifies the most intrinsically luminous AGN. (The two IR-only AGN with

$\log L_{\text{bol}}(\text{ergs s}^{-1}) < 44.5$ are the two IRAGN in Figure 1 with $z < 1$.)

3.5. Stellar Masses

To ensure that our morphological analysis is not biased by the underlying stellar mass distribution of the various AGN samples, we also plot in Figure 2 the distribution of stellar masses calculated using the techniques described in Santini et al. (2012), which take into account both the stellar and AGN contributions to the SED. As can be seen, there is no systematic offset between the stellar masses of the X-ray and IR-selected samples. Instead, as confirmed by KS tests between the full AGN sample and various subsamples, as well as between the IR-only and X-ray-only subsamples ($p\text{-value} = 0.46$), the AGN sub-samples are well-matched in stellar mass.

4. VISUAL MORPHOLOGIES

To determine the morphologies of our AGN sample, we utilized the CANDELS visual classification framework as described in Kartaltepe et al. (2015). For this study, the classification GUI displayed the Subaru V-band, HST ACS F814W (I-band), HST WFC3 F125W (J-band), and HST WFC3 F160W (H-band) images for each AGN. Twenty-one classifiers (all professional astronomers) then chose one or more of the following morphology classes for each AGN: disk, spheroid, peculiar/irregular, compact/point source, and unclassifiable. They then selected just one of the following interaction classes: merger, interaction within the segmen-

² We apply a correction factor to the X-ray luminosities from Marchesi et al. (2016a) to correct for a systematic offset between this catalog and Marchesi et al. (2016b) due to an inconsistency between the assumed spectral shapes (F. Civano 2017, private communication).

tation map, interaction outside the segmentation map, non-interacting companion, and no interaction. Classifiers also had the option of selecting from a number of flags, including tidal arms, double nuclei, asymmetric, and point source contamination. It is worth noting that while classifiers knew they were classifying a sample of AGN, they did not know which AGN were X-ray or IR-selected.

From these raw classifications, we created the following consensus classification categories for each source. For morphology, we added the asymmetric flag to our morphology classification (and flagged asymmetric in all cases where irregular had been chosen), resulting in the following non-mutually exclusive classes: disk, spheroid, irregular, point source (which also includes the point-source contamination flag), asymmetric, and unclassifiable. Following Kocevski et al. (2012), our consensus morphology class was then taken to be the combination of classes chosen by at least half (11+) of the classifiers. We show an example in Figure 3, where we plot the thumbnail images and individual morphology classifications for one of the IRAGN not detected in X-rays. In this particular case, the consensus morphology is Irregular+Asymmetric.

To determine the interaction class, we created the following five categories: undisturbed (no companion, interaction, merger, asymmetry, double nuclei, or tidal arms), undisturbed with a companion (companion, but no interaction, merger, asymmetry, double nuclei, or tidal arms), disturbed (no clear interaction or merger, but yes to asymmetry, double nuclei, or tidal arms), interaction or merger (either inside or outside the segmentation map), and unclassifiable. Our consensus interaction class was taken to be the most commonly selected of these five mutually-exclusive classes. In the example shown in Figure 3, nearly all of the classifiers agree that this particular AGN is in an interacting or merging system.

For those sources classified as interacting or merging, we then separated them into two additional subclasses: interacting/merging and disturbed (interactions/mergers where the asymmetric, double nuclei, or tidal arm flags had been selected as well) and interacting/merging yet relatively undisturbed (interactions/mergers where none of the asymmetric, double nuclei, or tidal arm flags were selected). In general, the latter class tends to catch early and/or wide separation mergers as well as minor mergers.

We plot in Figure 4 the WFC3 F160W thumbnail images of our AGN sample, broken down by interaction type, and also identify those AGN that are X-ray and/or infrared selected.

4.1. Morphology by AGN Type

We plot in Figure 5 two comparisons between the morphology and interaction classes for the X-ray and IR-selected AGN samples, where we separate the sample into IRAGN-only (no X-ray), X-ray+IRAGN, and X-ray only. The fractions for each category and subsample are given in Table 1.

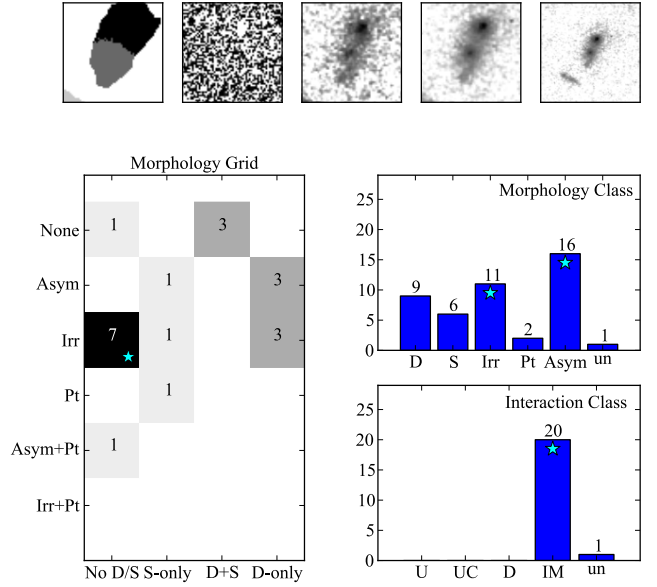
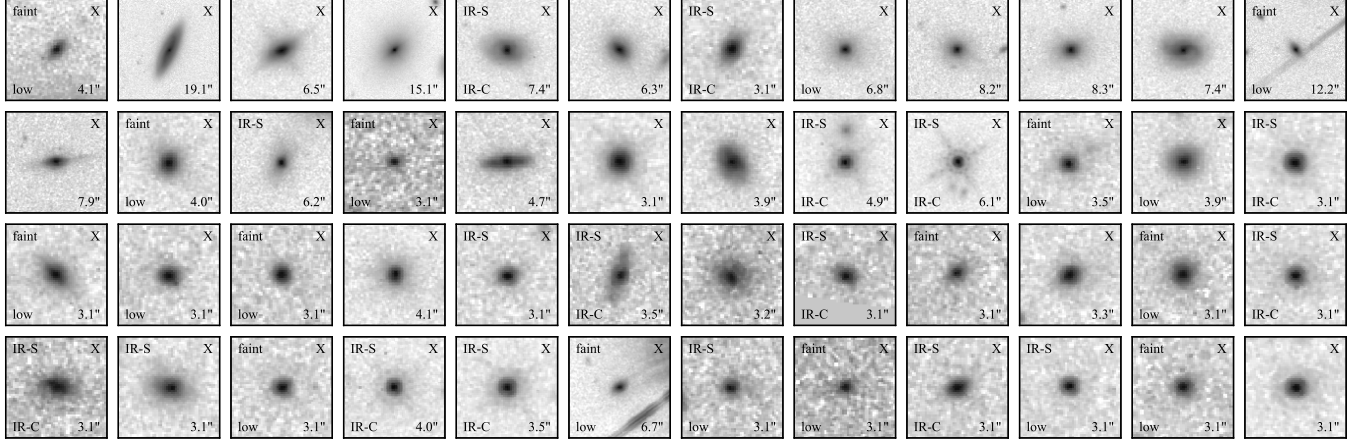


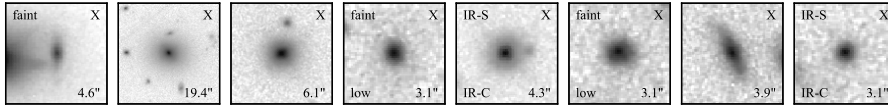
Figure 3. Morphology classification for one of the X-ray non-detected IRAGN. From left to right, the thumbnails at the top show the segmentation map along with the ACS F814W I-band image, WFC3 F125W J-band image, and WFC3 F160W H-band images both at the nominal size and twice that to identify nearby companions. The morphology grid shows the combination of classes (Disk, Spheroid, Asymmetric, Irregular, Point Source) chosen by each of the 21 classifiers. The histograms then show the morphology and interaction classes described in §4 (recall that all sources identified as irregular are also considered to be asymmetric). The final consensus classifications (morphology = Irregular/Asymmetric, interaction = Interacting/Merging) are given by cyan stars.

The figure on the left compares our full X-ray and Sanders et al. (2007)–selected IRAGN samples with one exception: we remove any AGN with a spectroscopic Type 1 identification to address the potential issue of rest-frame optical emission from the AGN masking the underlying morphology of the system. Removing the broad-line AGN (BLAGN) primarily impacts the unobscured, high-luminosity population that is both X-ray and IR-selected (15 AGN are known BLAGN, and 11 of these are also IRAGN). Of these 15 sources, 8 were classified as point sources by more than half of the classifiers, and 6 additional sources were classified as having a point source component by more than 20% of the classifiers. While it can occasionally be difficult for classifiers to distinguish between spheroids and point sources, the additional confirmation of a Type 1 spectrum indicates that we may not be seeing the underlying host galaxy emission in these systems. This restriction lowers the relative point source fraction for the X-ray+IR AGN sample and subsequently raises the fractions for the remaining morphologies.

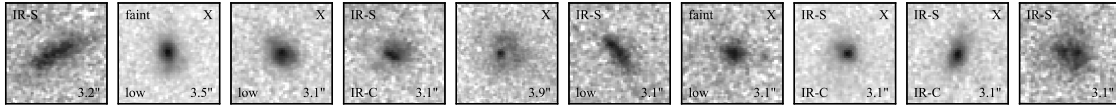
The figure on the right further restricts the IRAGN samples to those sources also selected using the COSMOS15 catalog (see §3.1). In this plot, we also remove any X-ray-only AGN that fall below our flux cuts in one or more of the Sanders et al. (2007) IRAC bands or that have $S/N < 3$ in one or more of the COSMOS15 IRAC bands.



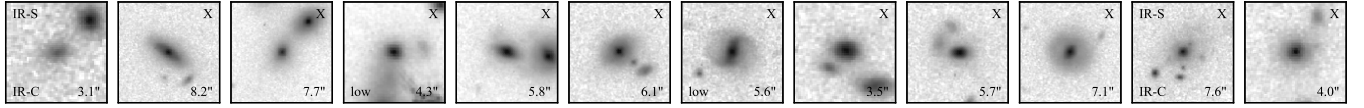
(a) Undisturbed



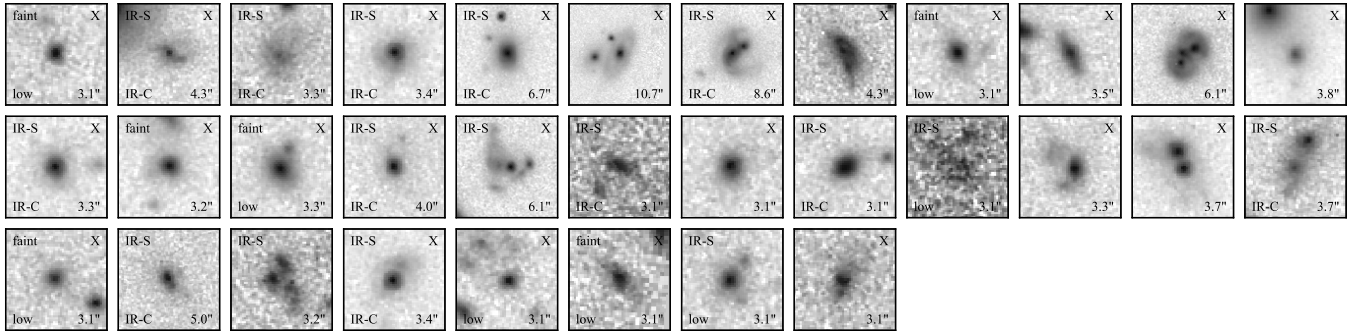
(b) Undisturbed with a Companion (some of which fall outside this field of view)



(c) Disturbed



(d) Interacting/Merging yet Relatively Undisturbed



(e) Interacting/Merging and Disturbed

Figure 4. WFC3 F160W thumbnail images for the X-ray and IR-selected AGN samples, broken down by the consensus interaction class. Sources detected in the X-ray have an ‘X’ in the upper right corner. IRAGN selected using [Sanders et al. \(2007\)](#) are indicated with an ‘IR-S’ in the upper left, where ‘faint’ means that the source falls below the IRAC detection limits in at least one band. IRAGN also selected using COSMOS15 are indicated with an ‘IR-C’ in the bottom left, where ‘low’ means that the source has $S/N < 3$ in at least one band. The diameter of each image is given in the lower right. Each thumbnail is scaled to the size of the galaxy with a minimum size of $3.1''$ (see [Kartaltepe et al. \(2015\)](#) for more details). It is worth noting that classifiers were shown thumbnails that match those shown here, as well as an H-band thumbnail twice as large to help identify potential companions.

Table 1. Percentage of AGN that meet Morphology and Interaction Classes

Class	Sanders et al. (2007) IR-only AGN	Sanders et al. (2007) IR+X-ray (no BLAGN)	X-ray-only AGN (no BLAGN)	COSMOS15 IR-only AGN	COSMOS15 IR+X-ray no BLAGN	X-ray-only AGN (restricted) ¹ no BLAGN
Number of Sources	16	16	64	9	12	33
Disk	38 ⁺¹³ ₋₁₀	44 ⁺¹² ₋₁₁	38 ⁺⁶ ₋₆	44 ⁺¹⁶ ₋₁₄	46 ⁺¹³ ₋₁₂	45 ⁺⁹ ₋₈
Spheroid	31 ⁺¹³ ₋₉	69 ⁺⁹ ₋₁₃	77 ⁺⁴ ₋₆	33 ⁺¹⁸ ₋₁₁	69 ⁺¹⁰ ₋₁₅	79 ⁺⁵ ₋₉
Irregular	50 ⁺¹² ₋₁₂	12 ⁺¹³ ₋₄	9 ⁺⁵ ₋₂	56 ⁺¹⁴ ₋₁₆	8 ⁺¹⁴ ₋₃	18 ⁺⁹ ₋₅
Point Source	6 ⁺¹² ₋₂	6 ⁺¹² ₋₂	2 ⁺³ ₋₀	11 ⁺¹⁸ ₋₄	8 ⁺¹⁴ ₋₃	0 ⁺⁵ ₋₁
Asymmetric	69 ⁺⁹ ₋₁₃	25 ⁺¹³ ₋₈	17 ⁺⁶ ₋₄	56 ⁺¹⁴ ₋₁₆	23 ⁺¹⁵ ₋₈	21 ⁺⁹ ₋₅
Unclassifiable	0 ⁺¹⁰ ₋₁	0 ⁺¹⁰ ₋₁	2 ⁺³ _{-0.0}	0 ⁺¹⁷ ₋₂	0 ⁺¹² ₋₁	0 ⁺⁵ ₋₁
Undisturbed	19 ⁺¹³ ₋₆	44 ⁺¹² ₋₁₁	45 ⁺⁶ ₋₆	22 ⁺¹⁸ ₋₈	38 ⁺¹⁴ ₋₁₁	39 ⁺⁹ ₋₈
Undisturbed + Companion	0 ⁺¹⁰ ₋₁	6 ⁺¹² ₋₂	8 ⁺⁵ ₋₂	0 ⁺¹⁷ ₋₂	8 ⁺¹⁴ ₋₃	9 ⁺⁸ ₋₃
Disturbed (D)	25 ⁺¹³ ₋₈	6 ⁺¹² ₋₂	6 ⁺⁵ ₋₂	11 ⁺¹⁸ ₋₄	8 ⁺¹⁴ ₋₃	3 ⁺⁶ ₋₁
Interacting/Merging	56 ⁺¹¹ ₋₁₂	44 ⁺¹² ₋₁₁	39 ⁺⁶ ₋₆	67 ⁺¹¹ ₋₁₈	46 ⁺¹³ ₋₁₂	48 ⁺⁹ ₋₈
Interacting/Merging, Undisturbed	6 ⁺¹² ₋₂	0 ⁺¹⁰ ₋₁	14 ⁺⁵ ₋₃	11 ⁺¹⁸ ₋₄	0 ⁺¹² ₋₁	21 ⁺⁹ ₋₅
Interacting/Merging and Disturbed (IMD)	50 ⁺¹² ₋₁₂	44 ⁺¹² ₋₁₁	25 ⁺⁶ ₋₅	56 ⁺¹⁴ ₋₁₆	46 ⁺¹³ ₋₁₂	27 ⁺⁹ ₋₆
IMD or D	75 ⁺⁸ ₋₁₃	50 ⁺¹² ₋₁₂	31 ⁺⁶ ₋₆	67 ⁺¹¹ ₋₁₈	54 ⁺¹² ₋₁₃	30 ⁺⁹ ₋₇

¹ The X-ray AGN in this column have been restricted to those sources that meet the [Sanders et al. \(2007\)](#) IRAC flux cuts and the COSMOS15 S/N cuts.

Because these X-ray AGN are faint in the IR, we cannot determine whether or not they would meet the IRAGN criteria. This restriction impacts only the X-ray-only sample and results in subtle changes to the morphology and interaction classes. In fact, we placed this restriction on the X-ray sources primary to illustrate the fact that it has little impact on the results, aside from increasing the binomial confidence error bars calculated using the method of [Cameron \(2011\)](#).

As can be seen from Figure 5, the main conclusions of this study are insensitive to whether the IRAGN are selected from [Sanders et al. \(2007\)](#) or COSMOS15. There are of course subtle differences between the two samples, and the lower sample size for the COSMOS15 IRAGN increases the error bars, but the trends discussed below hold regardless of the catalog we use to identify IRAGN.

Focusing first on the morphological classes, we see that the IR-only AGN, which tend to be heavily obscured, high-luminosity, and high-redshift AGN, are significantly more likely than X-ray-only AGN to have been classified as irregular (50⁺¹²₋₁₂% vs. 9⁺⁵₋₂%) or asymmetric (69⁺⁹₋₁₃% vs. 17⁺⁶₋₄%), and are significantly less likely to have been classified as having a spheroidal component (31⁺¹³₋₉% vs. 77⁺⁴₋₆%) (all at the $> 3\sigma$ level). Their disk fraction is indistinguishable from the other samples. As for their interaction class, these luminous, heavily-obscured AGN are less likely than X-ray-only AGN to be undisturbed (19⁺¹³₋₆% vs. 45⁺⁶₋₆%) and are more likely to be both ‘disturbed’ (25⁺¹³₋₈% vs. 6⁺⁵₋₂%), and

‘interacting/merging and disturbed’ (50⁺¹²₋₁₂% vs. 25⁺⁶₋₅%), though these differences are only significant at the $\sim 2\sigma$ level. However, if we combine those AGN classified as either ‘disturbed’, which may represent the late phases of a major merger, and ‘interacting/merging and disturbed’, we find that 75⁺⁸₋₁₃% of the IR-only AGN show signs of disturbance compared to only 31⁺⁶₋₆% of the X-ray-only sample, a difference that is significant at the 3σ level. The vast majority of our admittedly small sample of IR-only AGN therefore show signs of clear merger activity and/or disturbances that may be indicative of recent mergers. This indicates that major mergers may indeed play a dominant role in fueling high-luminosity, heavily-obscured AGN activity.

The morphologies and interactions classes of the AGN that meet both the X-ray and IRAGN criteria tend to fall between those of the X-ray-only and IR-only samples. This implies that while Seyfert-luminosity AGN are not predominantly associated with interacting and/or heavily disturbed hosts, the fraction of AGN with disturbed morphologies may increase at higher luminosities/redshifts (i.e. the X-ray+IR sample) or as the nuclear obscuration increases (IRAGN-only). We examine the independent impacts of luminosity and obscuration in §4.2.

Finally, it is worth noting that the increased merger fraction for our luminous, heavily obscured IR-only sample remains if we focus only on AGN in the fixed redshift range of $z = 1.5 - 2.5$ where a majority of IR-only AGN lie. Of

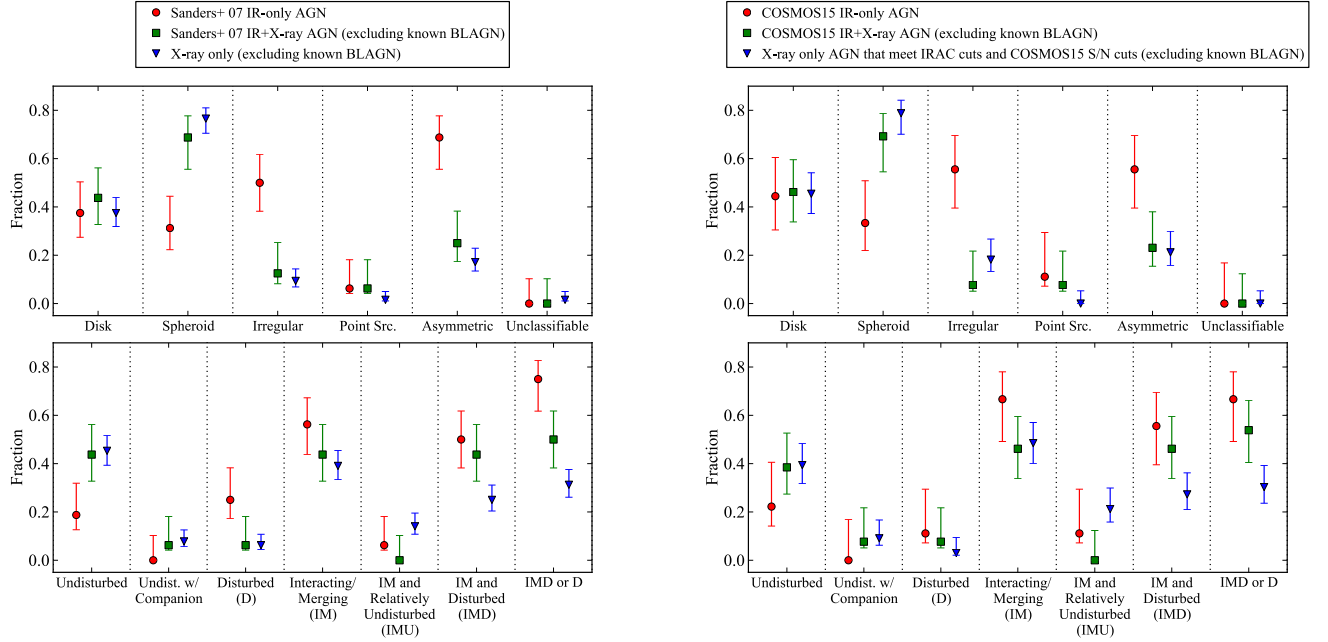


Figure 5. Comparison between the fraction of AGN in the various morphology (disk, spheroid, irregular, point source, asymmetric, and unclassifiable) and interaction (undisturbed, undisturbed with a companion, disturbed, interacting/merging, interacting/merging+relatively undisturbed, and interacting/merging and disturbed) classes, broken down by AGN sample (IR-only, IR+X-ray, X-ray-only). The plot on the left shows our full X-ray and Sanders et al. (2007)–selected IRAGN samples (with the exception of known BLAGN), whereas the plot on the right further restricts the IRAGN sample to those sources also identified using the COSMOS15 catalog and removes any X-ray AGN whose Sanders et al. (2007) IRAC fluxes or COSMOS15 S/N are too low to determine if they would meet the IRAGN selection criteria. Binomial confidence error bars are calculated using the method of Cameron (2011).

the 8 IR-only AGN in this redshift range (6 of which are selected both from the Sanders et al. (2007) and COSMOS15 catalogs), 6 (75%) are interacting or merging and disturbed. In contrast, only 2/12 X-ray+IR AGN (17%) are interacting (one is disturbed and the other is relatively undisturbed), and only 4/17 (24%) of the X-ray-only AGN are interacting (3 are disturbed, and one is relatively undisturbed). In this redshift range, obscuration (e.g., X-ray detected or not) appears to play a larger role than luminosity (e.g., IRAGN or not), though these results may be biased by the small number of sources. Nevertheless, the significantly higher merger fraction among luminous and obscured IR-only AGN in this limited redshift range suggests that the results for our full sample have not been highly biased by the larger average redshift of this sample compared to that of the X-ray selected AGN population.

4.2. Effects of Luminosity and Obscuration on Morphology

To determine if we can isolate the effects of luminosity and obscuration on the differences between the IR-only (high luminosity, heavily obscured) and X-ray only (lower luminosity, less obscured) populations, we plot in Figure 6 four of the the interaction classes as a function of both AGN bolometric luminosity (for luminosity bins with at least 5 AGN) and obscuration. We also plot the sum of AGN classified as either ‘interacting/merging and disturbed’ or simply ‘dis-

turbed’. For consistency with Figure 5, we exclude known BLAGN (see also §4.1).

The fraction of AGN classified as undisturbed appears to be independent of an AGN’s bolometric luminosity, and while the fraction that are interacting/merging *and* disturbed (IMD) increases with luminosity, this drops again in the highest luminosity bin. This drop is offset in part by a rise in AGN classified simply as disturbed (D) in the highest luminosity bin, such that the combination of ‘interacting/merging and disturbed’ plus ‘disturbed’ remains high at the highest luminosities. This trend is the opposite of those AGN classified as ‘interacting/merging yet relatively undisturbed’, which appear to be predominantly lower-luminosity Seyfert galaxies. However, luminosity and obscuration are not strictly independent in our sample: heavily obscured IR-only AGN comprise a significant fraction of the two highest luminosity bins, and our sample does not contain lower-luminosity AGN too obscured to be detected in the X-ray. It is therefore possible that the apparent increase in the disturbed fraction (IMD or D) at high luminosity is due at least in part to the heavily obscured IR-only AGN in our sample. Indeed, the rise in IMD+D with luminosity is still present but not as pronounced if we consider only the X-ray selected AGN.

Quantifying obscuration is somewhat more difficult than quantifying luminosity. Marchesi et al. (2016b) estimate X-ray column densities via X-ray spectral fitting for sources

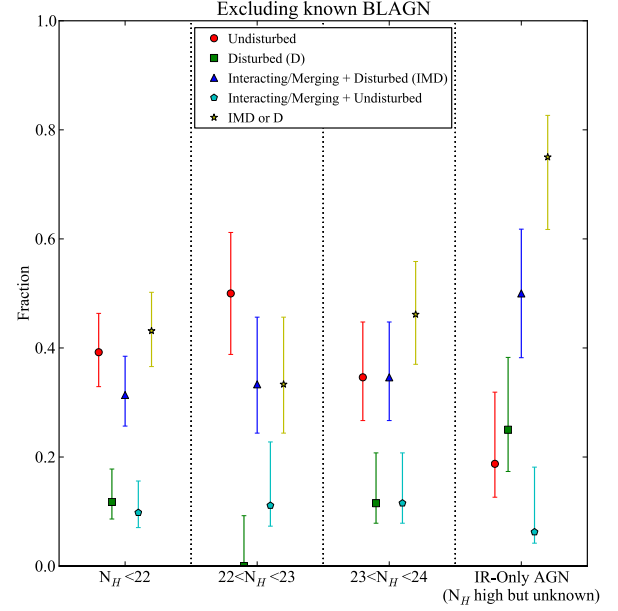
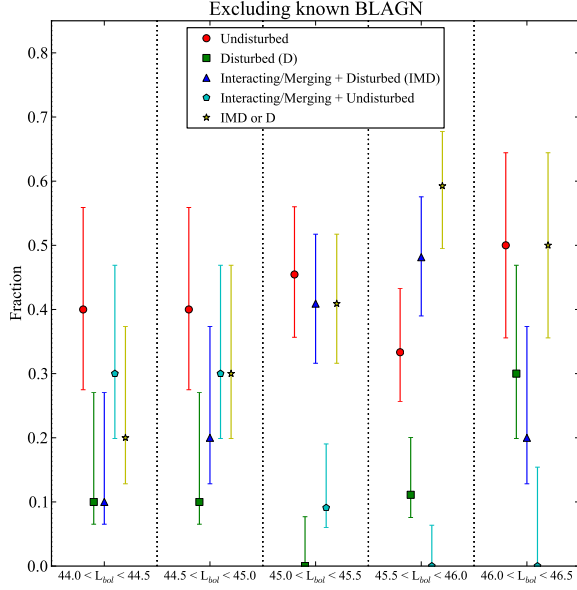


Figure 6. AGN interaction classes as a function of AGN bolometric luminosity in units of ergs s^{-1} (left) and AGN obscuration in units of $\log \text{cm}^{-2}$ (right). As in Figure 5, we exclude known BLAGN from the sample (see §4.1). While both luminosity and obscuration may impact the morphology of our sample, luminosity and obscuration are not strictly independent in our sample due to the inclusion of the IR-only AGN (high luminosity/high obscuration AGN). A larger and less biased sample is required to isolate the effects of luminosity and obscuration.

with > 30 counts in the 0.5-7 keV band, but only 55% of our X-ray sources meet this criterion. For the remaining X-ray sources, we adopt the column density estimates from [Marchesi et al. \(2016a\)](#) which are based on the observed X-ray hardness ratios (or limits on the hardness ratios). If only an upper limit is available (9% of the X-ray sample), we take this to be consistent with no obscuration, and in cases where only a lower limit is available (13% of the X-ray sample), we adopt this lower limit as our measure of N_H . Furthermore, while we expect that the X-ray non-detected IRAGN are heavily obscured, we do not know precisely how obscured they are. Given these limitations, we plot in Figure 6b the samples with $N_H < 10^{22}$, $10^{22} < N_H < 10^{23}$, $10^{23} < N_H < 10^{24}$, along with the IR-only AGN.

While the undisturbed fraction is lowest for the heavily obscured IR-only AGN, this trend is not statistically significant. Likewise, the ‘disturbed’ and ‘interacting/merging and disturbed’ fractions are highest for the IR-only population, but only marginally so, and while the sum of these disturbed categories (IMD+D) is highest for the IR-only AGN, there is no clear trend with obscuration for the X-ray detected AGN.

Disentangling the effects of luminosity and obscuration is therefore challenging, both due to our small sample size and the correlation between luminosity and obscuration, particularly for the IR-only subsample. It appears plausible that both luminosity and obscuration impact the morphology of our sample, but far more complete samples lacking a bias against

low-luminosity, heavily obscured AGN would be required to draw a definitive conclusion (see, for instance, [Kocevski et al. \(2015\)](#), who find that more heavily obscured AGN show an increase in disturbed morphologies.)

4.3. Comparison to Previous Results

We plot in Figure 7 the consensus morphology classes of our sample as a function of redshift/X-ray luminosity and IRAC color, and overplot the redshift and luminosity regimes sampled by the [Cisternas et al. \(2011b\)](#), [Silverman et al. \(2011\)](#), [Kocevski et al. \(2012\)](#), and [Kocevski et al. \(2015\)](#) studies. We see good agreement when we compare our morphology assessments to these prior studies. [Silverman et al. \(2011\)](#) found that $18\% \pm 8\%$ of $0.25 < z < 1.05$ Seyferts are in kinematic pairs (early mergers). Of the 16 AGN in our sample that meet their selection criteria, 7 (44%) are interacting. However, 2 of these are in late mergers and 1 is in a minor merger, for an early merger fraction of $4/16$, or 25%, consistent with the [Silverman et al. \(2011\)](#) result.

In a similar redshift regime that extends to both higher and lower luminosities, [Cisternas et al. \(2011b\)](#) found that 54% of AGN were undisturbed, 31% were mildly distorted, and 15% were strongly distorted. Of the 17 sources in our sample that meet their selection criteria, 9 (53%) are undisturbed, 3 (18%) are interacting/merging yet relatively undisturbed, and 5 (29%) are interacting/merging and disturbed. However, 2 of these interacting/merging and disturbed AGN are rela-

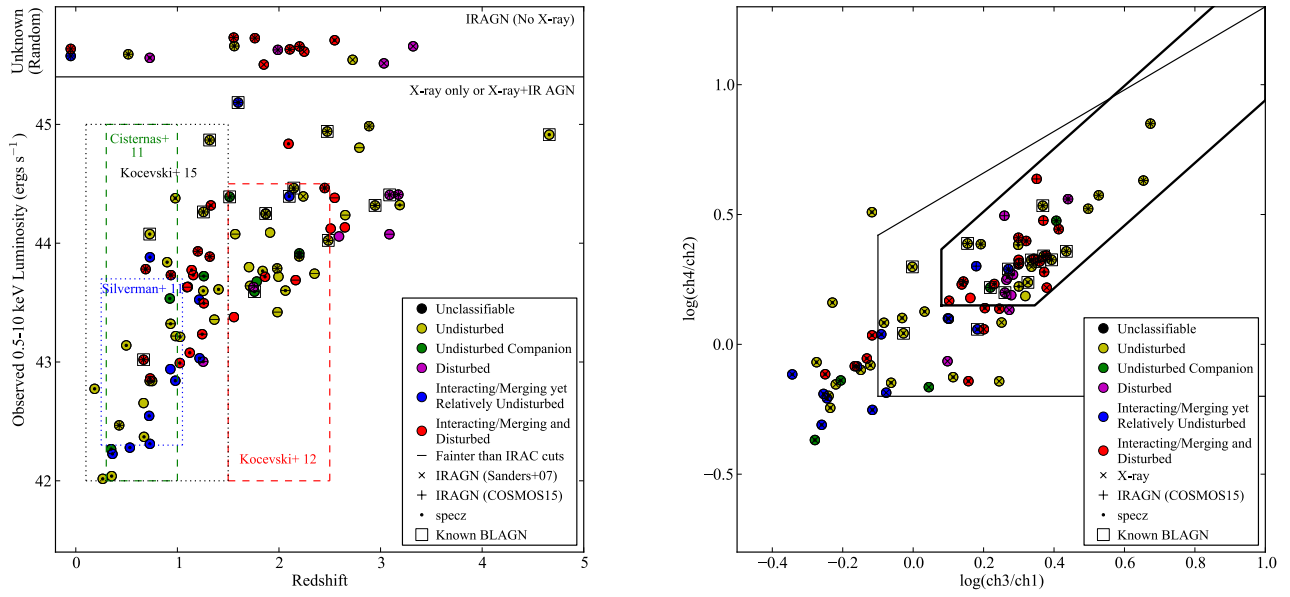


Figure 7. Consensus interaction class for our full sample as a function of both X-ray luminosity and redshift (left) and IRAC color (right). The regimes samples by several previous studies are shown as dotted lines. In addition to interaction class, we indicate those AGN that are X-ray or IR-detected, as well as those with spectroscopic redshifts and those known to be BLAGN. The AGN selection region from Donley et al. (2012) is plotted on the IRAC color plot on the right, as is the larger AGN wedge of Lacy et al. (2007).

tively minor disturbances that may have fallen in the ‘mildly distorted’ bin. Generally, we are again in good agreement with this prior study.

A direct comparison to the Kocevski et al. (2015) study of $z < 1.5$ X-ray selected AGN is difficult as their sample is split into subsamples with different X-ray obscurations, with each subsample covering a broad range of both luminosities and redshifts. If we focus only on their most obscured AGN with $N_H > 23.5 \text{ cm}^{-2}$ and compare to our IR-only sample that falls within the same redshift bounds, we see a larger merger fraction (50%) than they report (22%). However, our heavily-obscured IR-only AGN are predominantly quasars, whereas a significant fraction of their highly-obscured AGN have Seyfert-like luminosities. The higher merger fraction observed in our work may therefore be due to the systematically higher luminosity of our sample (see §1 and the references therein).

Finally, Kocevski et al. (2012) looked at the CANDELS morphologies of higher redshift X-ray AGN. They find that 19% of $L_x > 10^{43} \text{ erg s}^{-1}$ AGN are interacting/merging and 47% are undisturbed. Of the 26 sources in our sample that meet their selection criteria, 5 (19%) are interacting/merging, and 16 (62%) are undisturbed. We therefore conclude that our findings for lower luminosity and/or lower redshift AGN are consistent with findings in the literature that conclude that mergers do not play a dominant role in the fueling of Seyfert galaxies at either low ($z < 1$) or high ($z \sim 2$) redshift, even if

they may be responsible for driving AGN activity in higher luminosity, higher redshift, and more heavily obscured AGN.

4.4. Undisturbed Disks

Constraining the role of major mergers in fueling AGN activity can be complicated by a potential time delay between the merger and the peak of AGN activity. However, as disks are expected to be disrupted or destroyed by major mergers, the undisturbed disk fraction can be used to place a constraint on the fraction of AGN that are unlikely to have undergone a major merger, at least in the recent past. Of the X-ray-only AGN, 16% are classified as undisturbed galaxies with a disk component, as are a similar fraction (4/27, or 15%) of X-ray+IR AGN. Of the X-ray non-detected IRAGN, however, only 1/16 (6%) is undisturbed with a disk component. The fraction of relatively undisturbed disks is therefore low across our sample. However, a non-negligible fraction of both X-ray-only and X-ray+IR AGN lie in undisturbed disks, indicating that both moderate and high luminosity AGN activity can occur in the absence of any recent major interaction. The undisturbed disk fraction is even lower, however, for the IR-only AGN, suggesting that it may be less common for these AGN to be triggered in isolation.

5. CONCLUSIONS

In summary, using the deep CANDELS NIR imaging in the CANDELS/COSMOS field, we have compared the rest-frame visual morphologies of X-ray and IR-selected AGN.

The X-ray-only AGN in our sample cover a range of redshifts and tend to be Seyfert luminosity AGN with low to moderate obscuration. They are the least likely to be disturbed and the most likely to have a spheroidal component. When they are interacting or merging, the primary host galaxy often appears to remain relatively undisturbed, either because the merger is comparatively minor or because it is in an early phase more accurately described as a close pair. This suggests that low obscuration Seyfert luminosity activity either precedes the high-luminosity, heavily dust enshrouded phase predicted during a major merger (for close pairs that will later become a major merger), that low level AGN activity can be triggered by minor interactions, or that this activity is unrelated to the nearby companion. Our findings for the X-ray sample are consistent with past studies that have concluded that mergers are not a dominant source of fueling at low AGN luminosity and obscuration (e.g. [Kocevski et al. 2012](#); [Cisternas et al. 2011b](#); [Silverman et al. 2011](#)).

While stochastic fueling may account for Seyfert-luminosity AGN, models of galaxy and AGN formation suggests that major mergers are the dominant fueling mechanism for luminous, obscured AGN and their hosts (e.g. [Hopkins et al. 2008](#)). The IR-only AGN in our sample also span a range of redshifts, but unlike the X-ray-only sample, they tend to be high-luminosity, heavily obscured AGN. These AGN are significantly ($> 3\sigma$) more likely than X-ray-only AGN to have been classified as irregular or asymmetric and are also more likely than X-ray-only AGN (at the $\sim 2\sigma$ level) to be classified both as undergoing interactions/mergers that significantly disrupt the host galaxy and as simply ‘disturbed’, which could potentially indicate the late stages of a merger. Combining these two categories, we find that 75% of IR-only AGN show significant signs of disturbance compared to only 31% of the X-ray-only sample, a difference that is significant at the 3σ level. These results are consistent with theoretical models of galaxy and AGN growth as well as with recent observational evidence for an increase in the merger fraction at high luminosity and/or obscuration ([Guyon et al. 2006](#); [Kartaltepe et al. 2010](#); [Koss et al. 2012](#); [Treister et al. 2012](#); [Ellison et al. 2016](#); [Fan et al. 2016](#); [Koss et al. 2010](#); [Urrutia et al. 2012](#); [Satyapal et al. 2014](#); [Kocevski et al. 2015](#); [Ellison et al. 2016](#); [Shangguan et al. 2016](#); [Weston et al. 2017](#)).

The lack of evidence for merger-driven AGN growth in typical Seyfert-luminosity, X-ray selected AGN ([Schawinski et al. 2011](#); [Kocevski et al. 2012](#); [Simmons et al. 2012](#); [Sánchez et al. 2004](#); [Grogan et al. 2005](#); [Pierce et al. 2007](#); [Gabor et al. 2009](#); [Cisternas et al. 2011b](#); [Simmons et al. 2012](#); [Villforth et al. 2014](#); [Rosario et al. 2015](#); [Bruce et al. 2016](#)) can therefore be attributed to looking for mergers among the wrong population of AGN/hosts. By targeting luminous and heavily obscured AGN using IR selection, we have selected exactly the sample of AGN most likely to be merger driven, and indeed find evidence that the vast major-

ity are heavily disturbed.

JLD acknowledges support for this work provided by NASA through Hubble Fellowship grant HF-51303.01 awarded by the Space Telescope Science Institute, which is operated by the Association of Universities for Research in Astronomy, Inc., for NASA, under contract NAS5-26555. BDS acknowledges support from the National Aeronautics and Space Administration (NASA) through Einstein Postdoctoral Fellowship Award Number PF5-160143 issued by the Chandra X-ray Observatory Center, which is operated by the Smithsonian Astrophysical Observatory for and on behalf of NASA under contract NAS8-03060. CL acknowledges support from NSF grant AST-1004583. Finally, we thank the anonymous referee for discussions and comments that improved the paper.

REFERENCES

- Alexander, D. M., & Hickox, R. C. 2012, *New Astronomy Reviews*, 56, 93
- Alonso-Herrero, A., Pérez-González, P. G., Alexander, D. M., et al. 2006, *ApJ*, 640, 167
- Altamirano-Dévora, L., Miyaji, T., Aceves, H., et al. 2016, *RMxAA*, 52, 11
- Bahcall, J. N., Kirhakos, S., Saxe, D. H., & Schneider, D. P. 1997, *ApJ*, 479, 642
- Bennett, N., Canalizo, G., Jungwiert, B., et al. 2008, *ApJ*, 677, 846
- Bruce, V. A., Dunlop, J. S., Mortlock, A., et al. 2016, *MNRAS*, 458, 2391
- Brusa, M., Civano, F., Comastri, A., et al. 2010, *ApJ*, 716, 348
- Cameron, E. 2011, *Publications of the Astronomical Society of Australia*, 28, 128
- Canalizo, G., & Stockton, A. 2001, *ApJ*, 555, 719
- Cappelluti, N., Brusa, M., Hasinger, G., et al. 2009, *A&A*, 497, 635
- Cattaneo, A., Combes, F., Colombi, S., Bertin, E., & Melchior, A.-L. 2005, *MNRAS*, 359, 1237
- Cisternas, M., Jahnke, K., Bongiorno, A., et al. 2011a, *ApJL*, 741, L11
- Cisternas, M., Jahnke, K., Inskip, K. J., et al. 2011b, *ApJ*, 726, 57
- Civano, F., Elvis, M., Brusa, M., et al. 2012, *ApJS*, 201, 30
- Civano, F., Marchesi, S., Comastri, A., et al. 2016, *ApJ*, 819, 62
- Di Matteo, T., Springel, V., & Hernquist, L. 2005, *Nature*, 433, 604
- Donley, J. L., Rieke, G. H., Alexander, D. M., Egami, E., & Pérez-González, P. G. 2010, *ApJ*, 719, 1393
- Donley, J. L., Rieke, G. H., Pérez-González, P. G., & Barro, G. 2008, *ApJ*, 687, 111
- Donley, J. L., Rieke, G. H., Pérez-González, P. G., Rigby, J. R., & Alonso-Herrero, A. 2007, *ApJ*, 660, 167
- Donley, J. L., Koekemoer, A. M., Brusa, M., et al. 2012, *ApJ*, 748, 142
- Dunlop, J. S., McLure, R. J., Kucula, M. J., et al. 2003, *MNRAS*, 340, 1095
- Ellison, S. L., Patton, D. R., Mendel, J. T., & Scudder, J. M. 2011, *MNRAS*, 418, 2043
- Ellison, S. L., Teimoorinia, H., Rosario, D. J., & Mendel, J. T. 2016, *MNRAS*, 458, L34
- Engel, H., Tacconi, L. J., Davies, R. I., et al. 2010, *ApJ*, 724, 233
- Fan, L., Han, Y., Fang, G., et al. 2016, *ApJL*, 822, L32
- Gabor, J. M., Impey, C. D., Jahnke, K., et al. 2009, *ApJ*, 691, 705
- Gebhardt, K., Bender, R., Bower, G., et al. 2000, *ApJL*, 539, L13
- Glikman, E., Simmons, B., Mailly, M., et al. 2015, *ApJ*, 806, 218
- Greene, J. E., Zakamska, N. L., Liu, X., Barth, A. J., & Ho, L. C. 2009, *ApJ*, 702, 441
- Grogin, N. A., Conselice, C. J., Chatzichristou, E., et al. 2005, *ApJL*, 627, L97
- Guyon, O., Sanders, D. B., & Stockton, A. 2006, *ApJS*, 166, 89
- Hasinger, G. 2008, *A&A*, 490, 905
- Hasinger, G., Cappelluti, N., Brunner, H., et al. 2007, *ApJS*, 172, 29
- Hopkins, P. F., & Hernquist, L. 2006, *ApJS*, 166, 1
- . 2009, *ApJ*, 698, 1550
- Hopkins, P. F., Hernquist, L., Cox, T. J., et al. 2006, *ApJS*, 163, 1
- Hopkins, P. F., Hernquist, L., Cox, T. J., & Kereš, D. 2008, *ApJS*, 175, 356
- Hopkins, P. F., Kocevski, D. D., & Bundy, K. 2014, *MNRAS*, 445, 823
- Hopkins, P. F., Richards, G. T., & Hernquist, L. 2007, *ApJ*, 654, 731
- Ilbert, O., Capak, P., Salvato, M., et al. 2009, *ApJ*, 690, 1236
- Iverson, R. J., Smail, I., Amblard, A., et al. 2012, *MNRAS*, 425, 1320
- Kartaltepe, J. S., Sanders, D. B., Le Floch, E., et al. 2010, *ApJ*, 721, 98
- Kartaltepe, J. S., Mozena, M., Kocevski, D., et al. 2015, *ApJS*, 221, 11
- Kocevski, D. D., Faber, S. M., Mozena, M., et al. 2012, *ApJ*, 744, 148
- Kocevski, D. D., Brightman, M., Nandra, K., et al. 2015, *ApJ*, 814, 104
- Koekemoer, A. M., Faber, S. M., Ferguson, H. C., et al. 2011, *ApJS*, 197, 36
- Koss, M., Mushotzky, R., Treister, E., et al. 2012, *ApJL*, 746, L22
- Koss, M., Mushotzky, R., Veilleux, S., & Winter, L. 2010, *ApJL*, 716, L125
- Lacy, M., Petric, A. O., Sajina, A., et al. 2007, *AJ*, 133, 186
- Laigle, C., McCracken, H. J., Ilbert, O., et al. 2016, *ApJS*, 224, 24
- Larson, K. L., Sanders, D. B., Barnes, J. E., et al. 2016, *ApJ*, 825, 128
- Magorrian, J., Tremaine, S., Richstone, D., et al. 1998, *AJ*, 115, 2285
- Marchesi, S., Civano, F., Elvis, M., et al. 2016a, *ApJ*, 817, 34
- Marchesi, S., Lanzuisi, G., Civano, F., et al. 2016b, *ApJ*, 830, 100
- Mechtle, M., Jahnke, K., Windhorst, R. A., et al. 2016, *ApJ*, 830, 156
- Nayyeri, H., Hemmati, S., Mobasher, B., et al. 2017, *ApJS*, 228, 7
- Pierce, C. M., Lotz, J. M., Laird, E. S., et al. 2007, *ApJL*, 660, L19
- Reichard, T. A., Heckman, T. M., Rudnick, G., et al. 2009, *ApJ*, 691, 1005
- Robertson, B., Hernquist, L., Cox, T. J., et al. 2006, *ApJ*, 641, 90
- Rosario, D. J., McIntosh, D. H., van der Wel, A., et al. 2015, *A&A*, 573, A85
- Salvato, M., Ilbert, O., Hasinger, G., et al. 2011, *ApJ*, 742, 61
- Sánchez, S. F., Jahnke, K., Wisotzki, L., et al. 2004, *ApJ*, 614, 586
- Sanders, D. B., Soifer, B. T., Elias, J. H., et al. 1988, *ApJ*, 325, 74
- Sanders, D. B., Salvato, M., Aussel, H., et al. 2007, *ApJS*, 172, 86
- Santini, P., Rosario, D. J., Shao, L., et al. 2012, *A&A*, 540, A109
- Satyapal, S., Ellison, S. L., McAlpine, W., et al. 2014, *MNRAS*, 441, 1297
- Schawinski, K., Simmons, B. D., Urry, C. M., Treister, E., & Glikman, E. 2012, *MNRAS*, 425, L61
- Schawinski, K., Treister, E., Urry, C. M., et al. 2011, *ApJL*, 727, L31
- Shangguan, J., Liu, X., Ho, L. C., et al. 2016, *ApJ*, 823, 50
- Silverman, J. D., Kampczyk, P., Jahnke, K., et al. 2011, *ApJ*, 743, 2
- Simmons, B. D., Urry, C. M., Schawinski, K., Cardamone, C., & Glikman, E. 2012, *ApJ*, 761, 75
- Suh, H., Civano, F., Hasinger, G., et al. 2017, *ApJ*, 841, 102
- Treister, E., Schawinski, K., Urry, C. M., & Simmons, B. D. 2012, *ApJL*, 758, L39
- Urrutia, T., Lacy, M., & Becker, R. H. 2008, *ApJ*, 674, 80
- Urrutia, T., Lacy, M., Spoon, H., et al. 2012, *ApJ*, 757, 125
- Veilleux, S., Kim, D.-C., Rupke, D. S. N., et al. 2009a, *ApJ*, 701, 587
- Veilleux, S., Rupke, D. S. N., Kim, D., et al. 2009b, *ApJS*, 182, 628
- Villforth, C., Hamann, F., Rosario, D. J., et al. 2014, *MNRAS*, 439, 3342
- Villforth, C., Hamilton, T., Pawlik, M. M., et al. 2017, *MNRAS*, 466, 812
- Weston, M. E., McIntosh, D. H., Brodwin, M., et al. 2017, *MNRAS*, 464, 3882
- Zakamska, N. L., Strauss, M. A., Krolik, J. H., et al. 2006, *AJ*, 132, 1496